Kalman filter for integration of GNSS and InSAR data applied for monitoring of mining deformations

Damian Tondaś[1], Witold Rohm[1], Maya Ilieva[1], Jan Kapłon[1]

[1] Wrocław University of Environmental and Life Sciences, Poland (damian.tondas@upwr.edu.pl, witold.rohm@upwr.edu.pl, maya.ilieva@upwr.edu.pl, jan.kaplon@upwr.edu.pl)

Key words: *GNSS; InSAR; ground displacements; mining deformations; data integration; GNSS and InSAR fusion; Kalman filter*

ABSTRACT

Ground deformation monitoring can be performed using different measurement methods, e.g., leveling, gravimetry, photogrammetry, laser scanning, satellite navigation systems, Synthetic Aperture Radar (SAR), and others. In the presented study we introduced an original methodology of integration of the Differential Satellite Interferometric SAR (DInSAR) and Global Navigation Satellite Systems (GNSS) data using Kalman filter. However, technical problems related to invalid GNSS receivers functioning and noisy DInSAR results have a great impact on calculations provided only in the forward Kalman filter mode. To reduce the impact of unexpected discontinuity of observations, a backward Kalman filter was also introduced. The applied algorithm was tested in the Upper Silesian coal mining region in Poland. The paper presents the methodology of DInSAR and GNSS integration appropriate for small-scale and non-linear motions.

The verification procedure of the obtained results was performed using an external data source – GNSS campaign measurements. The overall RMS errors reached 18, 16, and 42 mm for the Kalman forward, and 19, 17, and 44 mm for the Kalman backward approaches in North, East, and Up directions, respectively.

I. INTRODUCTION

Over the years, the capabilities for determining land surface changes have developed significantly and also have found application in areas particularly affected by mining activities. However, none of the available methods for ground deformation monitoring applied separately can provide sufficient spatio-temporal resolution and high accuracy simultaneously. Hence, in this paper, we performed an original methodology for InSAR and GNSS data integration. The developed algorithm can be applied for small-scale non-linear dynamic deformations. To validate the proposed methodology, we used real observations performed in the Upper Silesian mining region in Poland.

The GNSS technology enables permanent monitoring of the surface movements in three-dimensional (3-D) space. Moreover, the evolution of GNSS processing techniques allows to determine positions with millimetre level accuracy and a latency ranging from a few seconds to less than one hour (Branzanti et al., 2013; Tondaś et al., 2020; Hadaś, 2015).

Unfortunately, the spatial range of the GNSS measurements concerns only the location where the geodetic antenna is mounted. Furthermore, to acquire a system for ground monitoring changes across an entire mine area, at least several dozen GNSS receivers are needed (Bian et al., 2014; Tao et al., 2018). Nowadays, to improve the spatial range of GNSS measurements, low-cost receivers are increasingly used. The most important aspect of using low-cost stations is to maintain the quality of the position determination. Various studies conducted for different types of low-cost receivers indicate sub-millimeter or millimeter differences compared to traditional geodetic GNSS stations (Cina et al., 2015; Hamza et al., 2021).

In contrast to the point-based GNSS technique, the InSAR areal investigations provide a better overview of local terrain changes. Moreover, some SAR products are freely available which significantly reduces the cost of ground deformation monitoring.

Nevertheless, InSAR methods also have some limitations related to (I) temporal resolution (a few days latency in acquiring a new image), (II) limited sensitivity to changes in the northern direction, (III) significant loss of coherence in vegetated areas depending on the radar wavelength, (IV) the impact of local atmospheric conditions brings additional radar signal delay and phase unwrapping problems. Furthermore, deformation can be acquired only in the 1-D line-of-sight (LOS) direction which substantially limits the capabilities to describe the detected surface deformation (Osmanoğlu et al., 2016; Fattahi et al., 2014).

Over past decades a great effort has been made to provide a unified solution for resolving the incomplete information for horizontal InSAR displacements. Hu et al. (2014) provide a systematic review of the methods for mapping 3-D displacements using InSAR measurements pointing out the strengths and weaknesses of each approach. The presented classification was categorized into three groups: (I) combination of multi-pass LOS and azimuth measurements, (II) integration of InSAR and GNSS data,

and (III) prior information assisted approaches. In our study, we refer to the second group of the mentioned methods - the integration of InSAR and GNSS.

Currently, the fusion process involves different approaches and assumptions for linear large-scale displacements or rapid non-linear movements. For instance, Liu et al. (2019) present a concept of linear interpolation and prediction based on the specific spatio-temporal domains. A new type of procedure to integrate InSAR and GNSS results was presented in the study of Boszo et al. (2021). The article shows a method for estimation of 3-D deformation parameters and rates using Sentinel-1 data and GNSS epoch observations converted to the LOS domain. The Kalman filter algorithm was tested on landslide area in Hungary with an assumption for linear velocities. To determine the 3-D deformation parameters, the GNSS data were projected onto the LOS vectors. The presented approach is based only on linear velocities calculated from two GNSS campaigns, thus in the last epoch, the calculated positions were rescaled using the GNSS-derived LOS values.

Based on the presented literature methods, it can be concluded that nowadays the GNSS-InSAR integration is suitable for large-scale linear motions. However, for small-scale non-linear deformations, current integration techniques are not well developed and robust against noise. For our study, we used GNSS observations from permanent ground stations and DInSAR deformation maps derived from Sentinel-1 data. Our algorithm is able to ingest the noisy GNSS NEU coordinates with significant gaps, and time series errors in the DInSAR ascending and descending LOS velocities due to troposphere artifact or improper SAR phase unwrapping. The observation uncertainties are rigorously determined from the parameter estimation process for GNSS data, while for DInSAR results the errors are calculated based on coherence values.

II. METHODOLOGY

The presented study was conducted for an area affected by underground mining works, for which two groups of data – DInSAR (Sections II.A) and GNSS (Sections II.B) are processed, aiming to achieve comprehensive monitoring of the ongoing ground deformations. A new approach for integration of the data using the Kalman filter is suggested in Section II.C To verify the obtained results, a quality analysis based on independent data set was performed (Section II.D).

A. *DInSAR processing*

In this study, a consecutive cumulative DInSAR manner for surface deformation monitoring is applied, where the second (slave) image of each interferogram is used as a primary (master) image in the next interferometric pair, forming continuous time series. A serious disadvantage is that this approach does not eliminate the contribution of the interferograms with lower quality. The DInSAR processing is accomplished with the Sentinel Application Platform (SNAP), provided by the European Space Agency (ESA), following the standard procedure. ESA's SAR Sentinel-1 data covering the area of interest acquired in Interferometric Wide swath (IW) mode with VV polarization are used. An external Digital Elevation Model (DEM), namely the 1-sec distribution of the Shuttle Radar Topography Mission (SRTM) Height file (Jarvis et al., 2008), is used for coregistration of the two images of each pair and for subtracting the stable topography component from the wrapped differential interferogram. The Goldstein non adaptive filter (Goldstein et al., 1998) was applied to enhance the two-dimensional phase unwrapping, done with the Statistical-Cost, Network-Flow Algorithm for Phase Unwrapping (SNAPHU, Chen et al., 2000). Finally, the values of the resulted unwrapped interferometric phase are transformed to the metric units.

To determine the error values of a particular pixel, the coherence coefficient was used to measure the phase noise. The phase variance is defined by the probability density functions depended on a multilook levels (Hanssen, 2001). In the presented study, the multilooking level is 1 ($L = 1$) and for single-look data, the phase variance can be expressed as:

$$\sigma^2_{\phi,L=1} = \frac{\pi^2}{3} - arcsin\pi(|\gamma|) + arcsin^2(|\gamma|) - -\frac{1}{2}\sum_{k=1}^{\infty}\frac{|\gamma|^{2k}}{k^2} \quad (1)$$

where σ_ϕ = phase noise
L = multilook level
γ = coherence coefficient
k = the index of summation

The final interferometric phase errors in the ascending and descending directions ($\sigma^A_{d_{los}}$, $\sigma^D_{d_{los}}$) are transformed into metric units:

$$\sigma_{d_{los}} = \frac{\lambda}{4\pi}\sigma_{\phi,L=1} \quad (2)$$

where $\sigma_{d_{LOS}}$= InSAR deformation error in LOS
λ = Sentinel-1 wavelength (~5.55 cm)

The deformation vector measured in the LOS direction can be described by the 3-D components as:

$$d_{los} = [sin(\theta)\, sin(\alpha) \; -sin(\theta)\, cos(\alpha) \;\; cos(\theta)] \begin{bmatrix} n_S \\ e_S \\ u_S \end{bmatrix} \quad (3)$$

where d_{LOS} = InSAR deformation in LOS
θ = incidence viewing angle
α = azimuth angle of Sentinel-1 satelitte
n_S, e_S, u_S= the SAR topocentric coordinates

B. *GNSS processing*

The coordinates of the permanent GNSS stations were estimated in post-processing mode using a double difference technique. The solution was based on United States' Global Positioning System (GPS), Russian Global

Navigation Satellite System (GLONASS), and ESA's Galileo observations with a daily computational interval. The processing executed in Bernese GNSS software v.5.2 (Dach et al., 2015) was carried out on the Center for Orbit Determination in Europe (CODE, Dach et al., 2018) final precision products. To ensure a stable reference, 14 stations belonging to the International GNSS Service (IGS) network and the European Reference (EUREF) Permanent Network (EPN) were included in post-processing calculations (Figure 1).

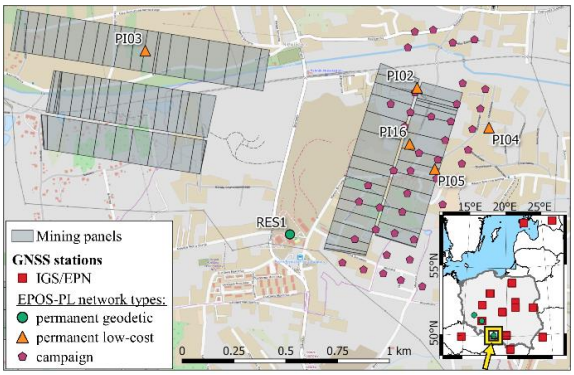

Figure 1. Map of the study area including undergoing mining exploitation panels (grey rectangles), locations of the permanent GNSS stations (green circles and orange triangles), and campaign points (purple pentagons). The map in the bottom right corner shows the locations of IGS/EPN reference stations (red squares)

In addition, independent epoch measurements were also considered in this paper. The GNSS campaign network containing over 100 points over the Upper Silesia region was developed for research purposes by the Military University of Technology in Warsaw (MUT). The MUT team processed the epochs of observations together with the GNSS data from the local network of the Continuously Operating Reference Station (CORS, Mutke et al., 2019).

The results obtained for the permanent and campaign GNSS points were determined in the ITRF2014 reference frame (Altamimi et al., 2016). To ensure consistency with the DInSAR data, which assume unchanging positions concerning the reference points, the ITRF2014 coordinates and uncertainties were transformed to the ETRF2000 frame using the 7-parameters conversion (Altamimi, 2018).

Afterwards, for a better understanding of the local displacements, the geocentric coordinates were converted to the topocentric NEU frame (Tao et al., 2018). The most illustrative way to present the position variation of the GNSS station over time is to take the first computational epoch as the reference value. To avoid the situation of adopting an outlier as an initial value for the permanent stations' time series, the averaged coordinates (N_G, E_G, U_G) from the first five computational observations were assumed as reference values. The reference for the positions of the campaigned GNSS points (N_C, E_C, U_C) were determined as the first common epoch with the data from the permanent stations.

C. *DInSAR and GNSS data integration*

The DInSAR measurements enable continuous monitoring of large-scale subsidence areas. However, the radar technique affords the observations in ascending and descending LOS directions. Whereas, the GNSS method provides determination of the displacements in 3-D, but only on sites where the antennas were located. Therefore, to perform the integration of small-scale displacements, it was necessary to overlay the DInSAR rasters with the GNSS locations. The information about implemented integration workflow is presented in Figure 2.

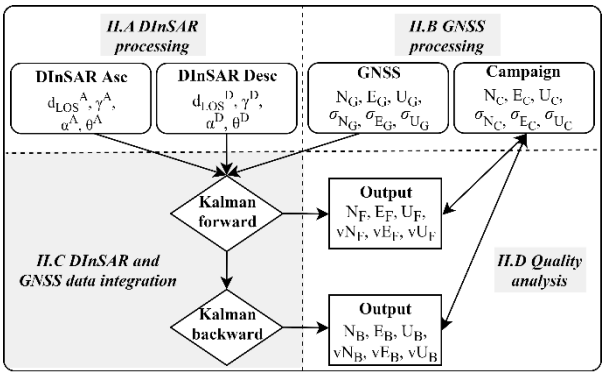

Figure 2. Scheme demonstrating the new method for applying DInSAR and GNSS observations (top part of the graph) in Kalman filter approaches (bottom left part of the graph) including quality analysis (bottom right part of the graph)

The process of integrating DInSAR and GNSS observations is based on the Kalman filter algorithm (Kalman, 1960). To estimate the unknown parameters and uncertainties of the system, the process follows as a recursive two-step procedure. In the first stage, termed as a *time-update*, to predict the parameters in the current epoch (t), information about the system from the previous epoch (t-*1*) is used. In the second step, named as a *measurement-update*, the modeled values, as well as the uncertainties, are corrected by the real observations and measurement noise received in the current epoch.

The *time-update* part of the DInSAR-GNSS integration contains the dynamic model for time-varying parameters (Verhagen et al., 2017). The state vector $\hat{x}$ is based on the three-dimensional values and velocities of ground deformations with a daily interval of calculation (Δt=1 day). The computations are conducted in the topocentric reference frame and the initial values ($\hat{x}_{0|0}$) are equal to zero. As the initial values of parameters errors ($P_{0|0}$) the system noise values are taken (S_t).

In our approach, the zero mean acceleration model is introduced as the system noise matrix (Teunissen, 2009):

$$S_t = \sigma_0^2 \begin{bmatrix} \frac{1}{4}\Delta t^4 & \frac{1}{2}\Delta t^3 & 0 & 0 & 0 & 0 \\ \frac{1}{2}\Delta t^3 & \Delta t^2 & 0 & 0 & 0 & 0 \\ 0 & 0 & \frac{1}{4}\Delta t^4 & \frac{1}{2}\Delta t^3 & 0 & 0 \\ 0 & 0 & \frac{1}{2}\Delta t^3 & \Delta t^2 & 0 & 0 \\ 0 & 0 & 0 & 0 & \frac{1}{4}\Delta t^4 & \frac{1}{2}\Delta t^3 \\ 0 & 0 & 0 & 0 & \frac{1}{2}\Delta t^3 & \Delta t^2 \end{bmatrix} \quad (6)$$

where σ_0 = the level of system noise

Δt = the interval of calculations

The σ_0 parameter was established empirically and the detailed results are presented in Section II.D.

The transition matrix ($\phi_{t|t-1}$) of the dynamic model describes the evolution of the state parameters in time, and can be obtained as a first-order differential equation:

$$\phi_{t|t-1} = \begin{bmatrix} 1 & \Delta t & 0 & 0 & 0 & 0 \\ 0 & 1 & 0 & 0 & 0 & 0 \\ 0 & 0 & 1 & \Delta t & 0 & 0 \\ 0 & 0 & 0 & 1 & 0 & 0 \\ 0 & 0 & 0 & 0 & 1 & \Delta t \\ 0 & 0 & 0 & 0 & 0 & 1 \end{bmatrix} \quad (7)$$

In the *measurement-update* step, to obtain a filtered system state with error variances, the prediction is combined with the actual observations in terms of minimum mean square error.

In the observations vector (z_t) the first three elements (N_G, E_G, U_G) refer to the topocentric position of the GNSS station received by processing with Bernese Software (Section II.B):

$$z_t = \begin{bmatrix} N_G & E_G & U_G & \frac{d^A_{LOS}}{\Delta T} & \frac{d^D_{LOS}}{\Delta T} \end{bmatrix}^T \quad (11)$$

The two last elements (d^A_{LOS}, d^D_{LOS}) are the differential LOS displacements obtained from the DInSAR ascending and descending geometries, respectively (Section II.A). The DInSAR observations were divided by the factor ΔT, which is the period of each interferogram, equal to 6, or 12 days in the case of a missing Sentinel-1 image.

In the projection matrix (A_t) the number of rows is equal to the number of measurements, while the number of columns determines the number of parameters

$$A_t = \begin{bmatrix} 1 & 0 & 0 & 0 & 0 & 0 \\ 0 & 0 & 1 & 0 & 0 & 0 \\ 0 & 0 & 0 & 0 & 1 & 0 \\ 0 & \sin(\theta^A)\sin(\alpha^A) & 0 & -\sin(\theta^A)\cos(\alpha^A) & 0 & \cos(\theta^A) \\ 0 & \sin(\theta^D)\sin(\alpha^D) & 0 & -\sin(\theta^D)\cos(\alpha^D) & 0 & \cos(\theta^D) \end{bmatrix} \quad (12)$$

The two last rows are related to the conversion of the NEU coordinates into the LOS domain (eq. 3). In the proposed model, GNSS observations describe displacement values, while the radar observations are considered as velocity measurements. The measurement noise matrix (R_t) contains the correlated variances of the GNSS topocentric coordinates ($\sigma_{N_G}, \sigma_{E_G}, \sigma_{U_G}, \sigma_{NE_G}, \sigma_{NU_G}, \sigma_{EU_G}$), whereas estimates calculated from the DInSAR in ascending and descending geometries are assumed to be uncorrelated ($\sigma_{d^A_{LOS}}, \sigma_{d^D_{LOS}}$):

$$R_t = \begin{bmatrix} \sigma^2_{N_G} & \sigma_{NE_G} & \sigma_{NU_G} & 0 & 0 \\ \sigma_{NE_G} & \sigma^2_{E_G} & \sigma_{EU_G} & 0 & 0 \\ \sigma_{NU_G} & \sigma_{EU_G} & \sigma^2_{U_G} & 0 & 0 \\ 0 & 0 & 0 & \sigma^2_{d^A_{LOS}} & 0 \\ 0 & 0 & 0 & 0 & \sigma^2_{d^D_{LOS}} \end{bmatrix} \quad (13)$$

The presented Kalman filter algorithm can be applied in a real-time mode and run anytime when a new observation appears. However, this method works only in a forward direction, so the detection and elimination of outliers which potentially occurred in the past is not possible. To get better estimates of the forward results, a backward Kalman filter could be applied (Figure 2).

The Kalman backward algorithm, named also as *smoothing processing*, relies on the forward Kalman filter results, but can also be used parallel to a real-time filter (Verhagen et al., 2017). The backward filter runs recursively with $t = \{N-1, N-2, \dots, 0\}$, where N is the current epoch. The smoothed state values ($\widehat{x^b}_{t|N}$) and error variance-covariance matrix ($P^b_{t|N}$).

The Kalman backward filter is mainly used in the post-processing mode. The *smoothing algorithm* cannot run separately – the results from the forward filter are required in every recursion. Finally, the statistical accuracy analysis was performed for the filtered forward ($N_F, vN_F, E_F, vE_F, U_F, vU_F$) and backward ($N_B, vN_B, E_B, vE_B, U_B, vU_B$) state vectors with respect to an external data source (Section II.D).

D. *Quality analysis*

To verify the obtained results, a quality analysis based on independent data set – GNSS campaign data (04.2019, 08.2019, 11.2019, 06.2020, 01.2021) that were realized in a common time span with the DInSAR and GNSS observations, was performed.

Due to the non-identical location of the campaign points with the permanent GNSS sites, the closest possible epoch-based point was selected for the verification. To ensure the co-location of the analysed time series, the offsets between coordinates were calculated. The 3-D shifts were eliminated based on the first common epoch for camping measurement and Kalman backward permanent data sets.

Moreover, to provide the most optimal σ_0 value of the Kalman system noise, RMS errors for 4 permanent stations were analysed regarding GNSS epoch measurements.

III. Deformation in active mine region: case study Rydultowy

The proposed new method of DinSAR-GNSS integration is tested for the area of the "Rydułtowy" mine, located in the south-western part of Upper Silesia in Poland, where the multilevel coal exploitation induces significant ground deformation and high seismicity. The area of interest is located in the immediate vicinity of the coal longwalls panels in the north-eastern part of the "Rydułtowy" mining area. In the expected deformation zones, a considerable number of GNSS receivers were positioned (Figure 1).

In the study area, one permanent geodetic GNSS station (RES1) was placed on the "Ignacy" Historical Mine. The station was not located directly above longwalls panels, however, ground deformations were expected. Five low-cost permanent receivers (PI02, PI03, PI04, PI05, PI16) were mounted to monitor terrain subsidence and lateral displacements during the exploitation of the "Rydułtowy" mine longwalls. The details about equipment and execution of the measurements are presented in Table 1.

Table 1. Classification of GNSS infrastructure deployed in Upper Silesia under the EPOS-PL project.

Name	Receiver	Antennas	Execution of measurements
geodetic RES1	Leica GR30	LEIAR20 LEIM	continuously, beginning 10.08.2018
low-cost PI02-PI05,PI16	Piksi Multi	HXCGPS500 NONE	continuously, beginning 11.02.2019
campaign 42 points	Trimble 5700	TRM39105.00, TRM41249.00	epoch-based, beginning Apr 2018

The beginning of collecting observations was 11.02.2019, however, due to technical problems, the low-cost time series are not complete (maximum break of around 9 months for PI02 station). Moreover, 42 campaign points were distributed over underground coal seams. The results of the measurements were used in the quality analyses. In order to co-locate with the low-cost permanent stations, a cross-reference was done with the nearest points – PI02, PI04, PI05, and PI16.

IV. Results

The methodology outlined in Section II.C was performed for two low-cost stations (PI16 and PI03 located just above active extraction panels) and one geodetic permanent station RES1 placed in the vicinity of the extraction panels (Figures 3-5). It has to be also noted that the integrated results are available for all six components: (N, E, U, vN, vE, vU), therefore each figure contains six panels – the first row is for the displacements, the second – for the velocities. The analysis of the graphical results is presented in Section IV.A and the details of the obtained residuals for low-cost permanent stations in the vicinity of campaign points are described in Section IV.B.

A. *Kalman filtering application*

The PI16 displacements visible in Figure 3. demonstrate that the epoch and permanent GNSS estimates follow a similar pattern, the North component (left panel) is undulating during the first nine months of the observations and then stabilize around 0.04 m. The East component (middle panel) is demonstrating similar displacement of 0.04 m for the first six months of 2020 and stabilize afterwards. The Up component (right panel) has a similar two-stage displacement cycle. In the first large significant event, lasting for the first nine months of the observations in 2019, introduces a vertical downlift of 0.30 m. During the second stage (the entire 202, the movement is rather slow – up to 0.40 m downlift. The Kalman forward model (green solid line) performs exceptionally well, tracing the estimated PI16 displacements in the North component (top row, left panel) epoch solution (the positive deformation is estimated to be 0.04 m at the last epochs of 03.2021). It is worth to note, that the GNSS permanent station demonstrates a noisy behavior in 06.2020. However, it has no impact on the Kalman filter, which produces stable outputs. Both East and Up components (top row, middle and right panels) forward filter estimates show a strong linear extrapolated trend past 06.2019 until 12.2019.

Velocities (the bottom row) that are taken from the DInSAR observations (dark blue dots in the middle and right panels) show very noisy output. It is interesting to mention, that the fast re-convergence of the Kalman filter fits to the GNSS results, once the GNSS data are available (data gap 06.2019 – 12.2019). The Kalman algorithm derived a good displacements alignment with the epoch solution, except for the last height estimated for 12.2020 (top row, right panel), which shows -0.35 m instead of -0.40 m. Backward Kalman filter as a smoothing solution aligns very well with the GNSS observations in all three components (top row, left, central and right panels), tracing the GNSS permanent solution.

Figure 4 demonstrates the fast changing station PI03, where the Kalman forward model (green solid line) predicts the movements in the North (left panel), East (central panel), and Up (right panel). The overall Kalman forward solution is tracing the GNSS observations, that transpire as a linear extrapolation sections visible in the long GNSS data gaps (06.2019 – 12.2019; 04.2020 – 06.2020). However, it is interesting to observe the quicker return to the tracing data trend in the case of the East component (middle panel), in 10.2019 – two months before the GNSS data reappear in the solution.

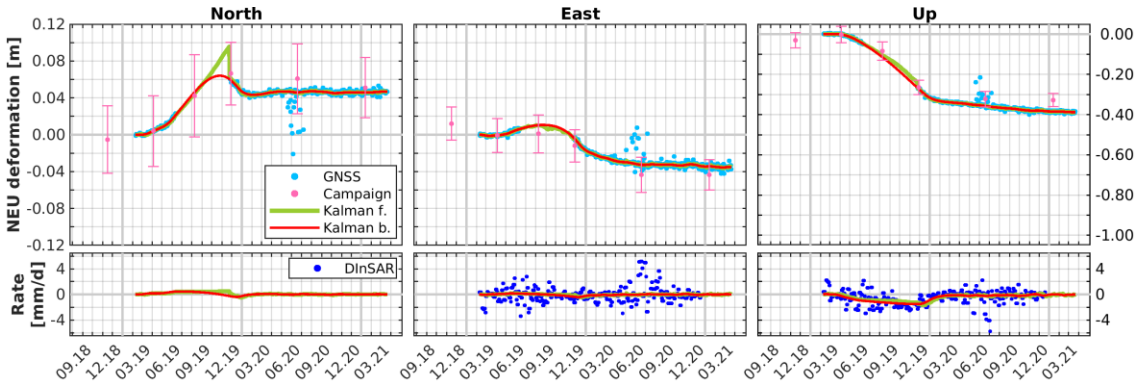

Figure 3. The displacement values (top row) and rates (bottom row) of the PI16 station are determined in the North (left panels), East (middle panels), and Up (right panels) directions. The charts present results of the GNSS permanent data (light blue dots), campaign GNSS measurements (pink dots with error bars), DInSAR data (dark blue dots), forward Kalman filter (green lines), and backward Kalman filter results (red lines).

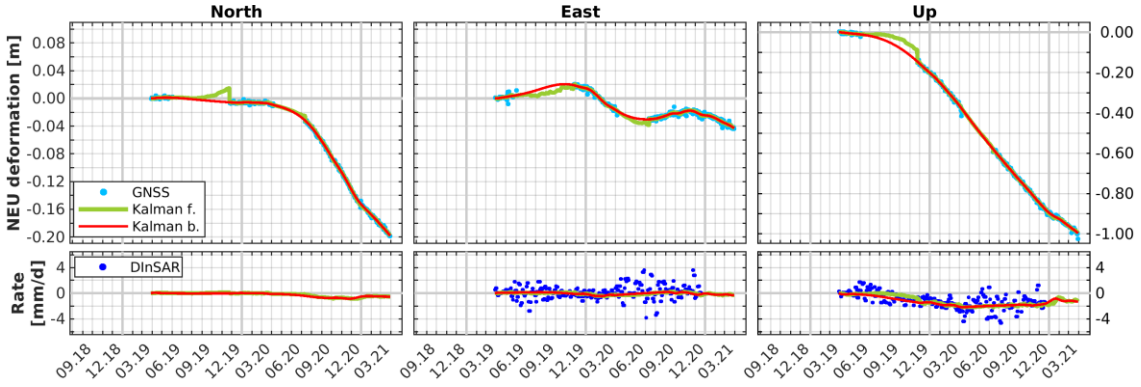

Figure 4. The displacement values (top) and rates (bottom) of the PI03 station are determined in the North (left panels), East (middle panels), and Up (right panels) directions. The legend is the same as in Figure 3

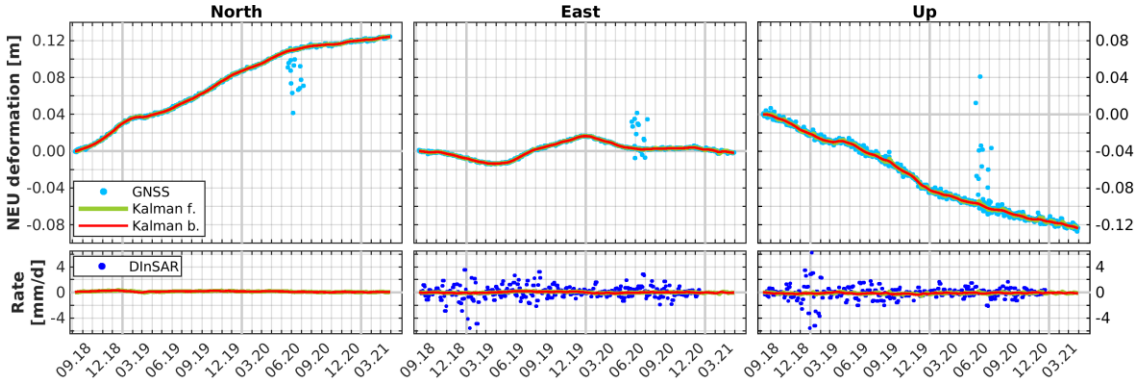

Figure 5. The displacement values (top) and rates (bottom) of the RES1 station are determined in the North (left panels), East (middle panels), and Up (right panels) directions. The legend is the same as in Figure 3

At the same time, the velocity estimated from the DInSAR data is much less noisy than the rest of the time series (bottom row, middle panel). It also has to be noted, that the velocities for the vertical component (bottom row, right panel), show significant negative values from DInSAR with noise low enough to make the trend estimation viable (up to 2 $\frac{mm}{day}$). The smoothed solution (backward Kalman filter – the red line), shows no significant jumps or breaks tracing the GNSS estimates very closely.

Figure 5 presents the Kalman filter estimates from DInSAR and GNSS for the RES1 station that is away from the major deformation zone and almost all GNSS data are available. It is clear that the Kalman filters, both forward and backward, are tracing the GNSS observations curve, while the DInSAR observations for this particular point do not bring any added value. Moreover, evaluating the bottom panels of Figure 5, it is clear to see, that the breaks in 2018 and 2019 brought a lot of noisy data that were difficult to process. Surprisingly, the Up component (right panel), demonstrates sections of different movement velocities aligned well with East component inflection points (03.2019 and 12.2019). The overall quality of the Kalman retrieval at the RES1 station could be taken as a reference for other sites.

Table.2 The North, East, and Up residuals for low-cost permanent stations in the vicinity of campaign points

				North		East		Up	
ID	Dist. to camp. pt. [m]	Max. Up displ. [mm]	Date	Kal. for. [mm]	Kal. back. [mm]	Kal. for. [mm]	Kal. back. [mm]	Kal. for. [mm]	Kal. back. [mm]
PI04	80	-201	04.19	-1	0	3	0	0	0
			08.19	-39	-38	12	15	84	85
			11.19	37	36	-2	-3	24	23
			06.20	2	2	34	34	75	75
			01.21	-34	-34	-20	-20	91	91
PI05	47	-270	04.19	-2	0	0	0	1	0
			08.19	12	19	-12	-12	6	-15
			11.19	4	0	-37	-38	26	20
			06.20	11	12	-5	0	14	7
			01.21	13	23	13	13	-18	-18
PI16	62	-388	04.19	0	0	0	0	1	0
			08.19	3	4	9	9	-22	-31
			11.19	-5	-7	8	7	-7	-8
			06.20	-15	-15	11	11	-33	-34
			01.21	-5	-5	9	9	-56	-56
Overall RMS				18	19	16	17	42	44

B. *Intersecting results*

The results presented in the previous sections demonstrate the capabilities of the application of the Kalman filtering in the integration concept for deformation monitoring. The subsequent analysis is based on the residual values for the GNSS permanent sites located in the vicinity of campaign points. The choice of the residual analysis against statistical evaluation is dictated by the small number of low-cost stations (PI04, PI02, PI05, and PI16), and the only 5 overlapping dates between the permanent and campaign points installation. Due to an insufficient number of samples (Chai et al., 2014), the calculation of any statistic based on five values was not robust. However, based on the calculated sets of differences in NEU directions the overall RMS errors were estimated (Table 2).

In Table 2, the discrepancies between the values for the campaign points and low-cost observations do not exceed 0.04 m for the North displacements (columns 5 and 6), however, the uncertainty of the campaign points is also 0.04 m. The overall RMS of the North component for the calculated residuals is 0.018 m and 0.019 m for the Kalman forward and backward approaches, respectively. In the East direction (columns 7 and 8), the discrepancies between the campaign points and the low-cost observations do not exceed 0.09 m, however, the uncertainty of the campaign points is 0.02 m. The RMS Kalman forward and backward filters are equal to 0.016 m and 0.017 m, respectively. There is no visible pattern in the magnitude of the residuals related to the distance to the campaign point (column 2).

The total displacement in the Up direction (column 3) is substantial and reaches -0.388 m (point PI16). The discrepancies between the campaign points and the low-cost observations do not exceed 0.16 m, however, the uncertainty of the campaign points is 0.03 m. The RMS for the Kalman forward and backward approaches are 0.042 m and 0.044 m, respectively. There is no visible pattern related to the maximum displacement (column 3) and the magnitude of residuals, however, the most significant values correspond to the longest distance between these points (column 2). For the PI04 station, the distance to the closest campaign point is 80 m and the three largest residual values are 0.091, 0.084, and 0.075 m for Kalman forward, and 0.091, 0.085, and 0.075 m for Kalman backward.

It is also worth to observe that the Kalman filters provide the solution across all reference epochs regardless of the GNSS missing data (see Figures 3-5).

The provided methodology is able to ingest the noisy GNSS NEU coordinates with significant gaps and the troposphere or unwrapping errors in the DInSAR data. The observation uncertainties are rigorously determined from the parameter estimation of the GNSS data, while for the DInSAR results the errors are calculated based on coherence coefficient values.

To obtain the most reliable Kalman filter results, the optimum noise level resolve of the system was essential (eq. 6). In our study, nine acceleration parameters were analysed with respect to the campaign measurements.

V. Conclusions

In the presented study, we introduced an original methodology for integrating DInSAR and GNSS data using the Kalman filter approach. This study concerns the "Rydułtowy" mine, located in the south-western part of Upper Silesia in Poland, where rapid ground deformations are observed. The cross-reference of the data sets is presented for stations PI16, PI03, and RES1. The nearest GNSS campaign sites were used to validate the results of the proposed integration for the permanent stations PI02, PI04, PI05, and PI16.

The lowest RMS error for the Kalman filter was obtained for the acceleration level of 0.05 $\frac{mm}{day^2}$.

Furthermore, detection and elimination of any potential outliers in the past, using the forward Kalman filter, is not possible. In order to get better integration results, backward Kalman filter was also applied. In comparison to the campaign GNSS results, the overall RMS errors reached 18, 16, 42 mm for Kalman forward and 19, 17, 44 mm for Kalman backward in North, East, Up directions, respectively. The fusion processing may be easily extended by other data sources like, e.g., Permanent Scatterer InSAR, leveling, or LiDAR, to create a framework for multi-sensor ground deformation monitoring system.

VI. Acknowledgements

This study was started in 2016 in the frames of the EPOS-PL project POIR.04.02.00-14-A003/16, and continued in 2021-2022 within the EPOS-PL+ project POIR.04.02.00-00-C005/19-00, that were funded by the Operational Program Smart Growth 2014–2020, Priority IV: Increasing research potential, Action 4.2: Development of modern research infrastructure in the science sector.

The presented investigation was accomplished as part of a scientific internship at Delft University of Technology (TU Delft), Netherlands, conducted within the GATHERS project, funded by the European Union's Horizon 2020 research and innovation programme under grant agreement No 857612. The authors would like to express their gratitude to Freek van Leijen and Hans van der Marel from TU Delft for the valuable guidance and discussions.

References

Altamimi, Z.: EUREF Technical Note 1: Relationship and Transformation between the International and the European Terrestrial Reference Systems. EUREF Technical Note 1: Version June 28, 2018 p. 11 (2018)

Altamimi, Z., Rebischung, P., Métivier, L., Collilieux, X.: ITRF2014: A new release of the International Terrestrial Reference Frame modeling nonlinear station motions. Journal of Geophysical Research: Solid Earth (2016)

Bian, H.F., Zhang, S.B., Zhang, Q.Z., Zheng, N.S.: Monitoring large-area mining subsidence by GNSS based on IGS stations. Transactions of Nonferrous Metals Society of China (English Edition) 24(2), 514–519 (2014).

Bozso, I., Banyai, L., Hooper, A., Szucs, E., Wesztergom, V.: Integration of Sentinel-1 Interferometry and GNSS Networks for Derivation of 3-D Surface Changes. IEEE Geoscience and Remote Sensing Letters (2021).

Branzanti, M., Colosimo, G., Crespi, M., Mazzoni, A.: GPS near-real-time coseismic displacements for the great tohoku-oki earthquake. IEEE Geoscience and Remote Sensing Letters 10(2), 372–376 (2013).

Chai, T., Draxler, R.R.: Root mean square error (RMSE) or mean absolute error (MAE)? -Arguments against avoiding RMSE in the literature. Geoscientific Model Development 7(3), 1247–1250 (2014).

Chen, C.W., Zebker, H.A.: Network approaches to two-dimensional phase unwrapping: Intractability and two new algorithms. Journal of the Optical Society of America (2000)

Cina, A., Piras, M.: Performance of low-cost GNSS receiver for landslides monitoring: test and results. Geomatics, Natural Hazards and Risk 6(5-7), 497–514 (2015).

Dach, R., Lutz, S., Walser, P., Fridez, P.: Bernese GNSS Software version 5.2. User manual. Astronomical Institute, University of Bern (2015).

Dach, R., Schaer, S., Arnold, D., Prange, L., Sidorov, D., Stebler, P., Villiger, A., Jäggi, A.: CODE final product series for the IGS. Astronomical Institute, University of Bern (2018).

Fattahi, H., Amelung, F.: InSAR uncertainty due to orbital errors. Geophysical Journal International (2014).

Goldstein, R.M., Werner, C.L.: Radar interferogram filtering for geophysical applications. Geophysical Research Letters 25(21), 4035–4038 (1998).

Hadaś, T.: GNSS-Warp Software for Real-Time Precise Point Positioning. Artificial Satellites 50(2), 59–76 (2015).

Hamza, V., Stopar, B., Sterle, O.: Testing the performance of multi-frequency low-cost gnss receivers and antennas. Sensors 21(6), 1–16 (2021).

Hanssen, R.: Radar interferometry: data interpretation and error analysis. Springer Science & Business Media (2001).

Hu, J., Li, Z.W., Ding, X.L., Zhu, J.J., Zhang, L., Sun, Q.: Resolving three-dimensional surface displacements from InSAR measurements: A review. Earth-Science Reviews (2014).

Jarvis, A., Reuter, H.I., Nelson, A., Guevara, E.: Hole-filled seamless SRTM data V4, International Centre for Tropical Agriculture (CIAT). Tech. rep. (2008)

Kalman, R.E.: A New Approach to Linear Filtering and Prediction Problems. Journal of Basic Engineering (1960).

Liu, N., Dai, W., Santerre, R., Hu, J., Shi, Q., Yang, C.: High Spatio-Temporal Resolution Deformation Time Series with the Fusion of InSAR and GNSS Data Using Spatio-Temporal Random Effect Model. IEEE Transactions on Geoscience and Remote Sensing 57(1), 364–680 (2019).

Mutke, G., Kotyrba, A., Lurka, A., Olszewska, D., Dykowski, P., Borkowski, A., Araszkiewicz, A., Barański, A.: Upper Silesian Geophysical Observation System A unit of the EPOS project. Journal of Sustainable Mining 18(4), 198–207 (2019).

Osmanoğlu, B., Sunar, F., Wdowinski, S., Cabral-Cano, E.: Time series analysis of InSAR data: Methods and trends. ISPRS Journal of Photogrammetry and Remote Sensing (2016).

Tao, T., Liu, J., Qu, X., Gao, F.: Real-time monitoring rapid ground subsidence using GNSS and Vondrak filter. Acta Geophysica 67(1), 133–140 (2018).

Teunissen, P.: Dynamic data processing: Recursive least-squares (2009)

Tondaś, D., Kapłon, J., Rohm, W.: Ultra-fast near real-time estimation of troposphere parameters and coordinates from GPS data. Measurement p. 107849 (2020).

Verhagen, S., Teunissen, P.J.: Least-Squares Estimation and Kalman Filtering. Springer Handbooks pp. 639–660 (2017).